

# Optical and X-ray discovery of the changing-look AGN IRAS 23226-3843 showing extremely broad and double-peaked Balmer profiles

W. Kollatschny<sup>1</sup>, D. Grupe<sup>2</sup>, M.L. Parker<sup>3</sup>, M. W. Ochmann<sup>1</sup>, N. Schartel<sup>3</sup>, E. Herwig<sup>1</sup>, S. Komossa<sup>4</sup>, E. Romero-Colmenero<sup>5</sup>, M. Santos-Lleo<sup>3</sup>

<sup>1</sup> Institut für Astrophysik, Universität Göttingen, Friedrich-Hund Platz 1, D-37077 Göttingen, Germany  
e-mail: wkollat@astro.physik.uni-goettingen.de

<sup>2</sup> Department of Physics, Earth Sciences, and Space System Engineering, Morehead State University, Morehead, KY 40351, USA

<sup>3</sup> XMM-Newton Science Operations Centre, ESA, Villafranca del Casuntilo, Apartado 78, 28691 Villanueva de la Cañada, Spain

<sup>4</sup> Max-Planck-Institut für Radioastronomie, Auf dem Hügel 69, D-53121 Bonn, Germany

<sup>5</sup> South African Astronomical Observatory, P.O. Box 9, Observatory 7935, Cape Town, South Africa

Received March 6, 2020; Accepted March 28, 2020

## ABSTRACT

**Aims.** We detected a very strong X-ray decline in the galaxy IRAS 23226-3843 within the XMM-Newton slew survey in 2017. Subsequently, we carried out multi-band follow-up studies to investigate this fading galaxy in more detail.

**Methods.** We took deep follow-up *Swift*, XMM-Newton, and NuSTAR observations in combination with optical SALT spectra of IRAS 23226-3843 in 2017. In addition, we reinspected optical, UV, and X-ray data that were taken in the past.

**Results.** IRAS 23226-3843 decreased in X-rays by a factor of more than 30 with respect to ROSAT and *Swift* data taken 10 to 27 years before. The broadband XMM-Newton/NuSTAR spectrum is power-law dominated, with a contribution from photoionized emission from cold gas, likely the outer accretion disk or torus. The optical continuum decreased by 60% and the Balmer line intensities decreased by 50% between 1999 and 2017. The optical Seyfert spectral type changed simultaneously with the X-ray flux from a clear broad-line Seyfert 1 type in 1999 to a Seyfert 1.9 type in 2017. The Balmer line profiles in IRAS 23226-3843 are extremely broad. The profiles during the minimum state indicate that they originate in an accretion disk. The unusual flat Balmer decrement  $H\alpha/H\beta$  with a value of 2 indicates a very high hydrogen density of  $n_H > 10^{11} \text{ cm}^{-3}$  at the center of the accretion disk. IRAS 23226-3843 shows unusually strong FeII blends with respect to the broad line widths, in contrast to what is known from Eigenvector 1 studies.

**Key words.** Galaxies: active – Galaxies: Seyfert – Galaxies: nuclei – Galaxies: individual: IRAS 23226-3843 – (Galaxies:) quasars: emission lines

## 1. Introduction

It is generally known that Seyfert 1 galaxies are variable in the optical and in X-ray continua on timescales of hours to decades. Several active galactic nuclei (AGN) have shown variability amplitudes by a factor of more than 20 in the X-rays (e.g., Grupe et al. 2001, 2010). AGN that show extreme X-ray flux variations in combination with X-ray spectral variations, that is, when a Compton-thick AGN becomes Compton-thin and vice versa, are called changing-look AGN (e.g., Guainazzi 2002). By analogy, optical changing-look AGN exhibit transitions from type 1 to type 2 and vice versa. In this case, the optical spectral classification can change as a result of a variation in the accretion rate, accretion disk instabilities, or a variation in reddening.

To date, a few dozen Seyfert galaxies are known to have changed their optical spectral type, for example, NGC 3516 (Collin-Souffrin et al. 1973), NGC 7603 (Tohline & Osterbrock 1976, Kollatschny et al. 2000), NGC 4151 (Penston & Perez 1984), Fairall 9 (Kollatschny et al. 1985), NGC 2617 (Shappee et al. 2014), Mrk 590 (Denney et al. 2014), HE 1136-2304 (Parker et al. 2016, Zetzl et al. 2018, Kollatschny et al. 2018), and IES 1927+654 (Trakhtenbrot et al. 2019, and references therein). Further recent findings are based on spectral variations detected by means of the Sloan Digital Sky Survey (SDSS) (e.g.,

Komossa et al. 2008, LaMassa et al. 2015, Rumbaugh et al. 2018, MacLeod et al. 2019), the Catalina Real-time Transient Survey (Graham et al. 2020), or the Wide-field Infrared Survey Explorer (Stern et al. 2018). In most of these recent findings, only a few optical spectra of the individual SDSS galaxies have been secured to prove their changing-look character. Other studies tried to detect correlations of the optical variability amplitudes with spectral properties, such as emission line widths (Kollatschny et al. 2006).

Initially, IRAS 23226-3843 was listed as a bright X-ray source in the RASS catalog (e.g., Grupe et al. 2001). Other designations for IRAS 23226-3843 are CTS B11.01, 2MASX J23252420-3826492, 6dF J2325242-382649, and HE 2322-3843. It was included in the NRAO VLA Sky Survey (NVSS) as a radio source with a flux density level of 4.3 mJy (Condon et al. 1998). IRAS 23226-3843 was classified as Seyfert type 1 in 1991 (Allen et al. 1991) based on its optical spectrum. The galaxy is of morphology type SO (Loveday 1996). Figure 1 displays the 6dF B-band image of IRAS 23226-3843 (scale: 1 x 1 arcmin corresponding to 41 x 41 kpc) (Jones 2004). An apparent magnitude of  $13.38 \pm 0.10$  was measured for this object in the R band in the Las Campanas Redshift Survey (1991-1996) (Schech-

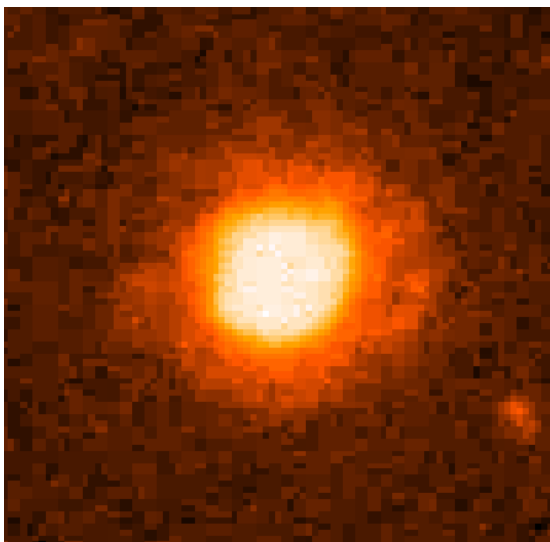


**Fig. 1.** 6dF B-band image of the S0-type galaxy IRAS 23226-3843. Scale: 1 x 1 arcmin. North is to the top, east to the left.

man et al. 1996). This corresponds to an absolute magnitude of  $M_R = -22.33 \pm 0.10$  mag.

We detected a very strong X-ray decrease in IRAS 23226-3843 within the XMM-Newton slew survey in 2017. Thereupon, we carried out optical and X-ray follow-up studies to investigate this galaxy in more detail and to study its variability behavior. Extreme cases of Seyfert-type changes like those in IRAS 23226-3843 provide us with tight constraints on the accretion physics and accretion disk changes on short timescales.

Throughout this paper, we assume a  $\Lambda$ CDM cosmology with a Hubble constant of  $H_0 = 73 \text{ km s}^{-1} \text{ Mpc}^{-1}$ ,  $\Omega_\Lambda = 0.73$ , and  $\Omega_M = 0.27$ . With a redshift of  $z = 0.0359$ , this results in a luminosity distance of  $D_L = 144 \text{ Mpc}$ .

## 2. Observations and data reduction

IRAS 23226-3843 ( $\alpha_{2000} = 23^{\text{h}} 25^{\text{m}} 24.2^{\text{s}}$ ,  $\delta = -38^\circ 26' 49.2''$ ) was found to be a variable X-ray source by the XMM-Newton slew survey in April, 2017. The 0.2–2 keV flux decreased by a factor of about 10 in comparison to ROSAT all-sky survey data in 1990. The ROSAT flux in 1990 amounted to  $1.85 \pm 0.18 \times 10^{-11} \text{ cm}^{-2} \text{ s}^{-1}$  (0.1–2.4 keV) (Mahony et al. 2010). We started a variability campaign with *Swift* after detecting the decreasing X-ray flux in 2017 April. In addition, we carried out follow-up XMM-Newton and NuSTAR observations as part of a ToO program to study extreme variable X-ray sources. Furthermore, we took optical spectra of IRAS 23226-3843 with SALT to investigate the optical spectral variations.

### 2.1. X-ray, UV, and optical continuum observations with *Swift*

After the discovery of the decreasing X-ray flux in 2017 April, we started monitoring IRAS 23226-3843 with *Swift* (Gehrels et al. 2004) in X-rays and the UV/optical. All *Swift* observing dates and exposure times are listed in Table A.1. In addition, IRAS 23226-3843 has been observed before by *Swift* during three epochs in 2007, 2008–2009, and 2013. For comparison purposes, we list these observations in all the tables relevant to *Swift* data (see Tables A.1, A.2, and A.3).

All X-ray observations with the *Swift* X-ray Telescope (XRT, Burrows et al. 2005) were performed in photon-counting mode (pc-mode, Hill et al. 2004). During the high state at the beginning of the observations in 2007–2013, source counts were collected in a circular region with a radius of 30 pixels (equivalent to  $70''$ ) and background counts in a nearby source-free circular region with a radius of 90 pixels (equal to  $210''$ ). For the low-state observations in 2016–2017, we used  $47''$  (20 pixel) and  $235''$  (100 pixel) extraction radii for the source and background counts, respectively. Spectra were extracted with the FTOOL *XSELECT*. An auxiliary response file (ARF) was created for each observation using *xrtmkarf*. We applied the *Swift* XRT response file *swxpc0to12s6\_20130101v014.rmf*.

Most spectra were rebinned to have at least 20 counts per bin using *grppha*. For low-state spectra, however, the number of counts was too low to allow  $\chi^2$  statistics. These data were fit by Cash statistics (Cash 1979) as indicated in Table A.3. The spectral analysis was performed in *XSPEC* (Arnaud 1996). All spectra were fit with a single power-law model with Galactic absorption ( $N_{\text{H,gal}} = 1.59 \times 10^{20} \text{ cm}^{-2}$ ; Kalberla et al. 2005).

Count rates, hardness ratios, and the best-fit values obtained are listed in Table A.3. The hardness ratio is defined as  $HR = \frac{H-S}{H+S}$ , where  $S$  = counts(0.3–1.0 keV) and  $H$  = counts(1.0–10.0 keV). In order to determine a background-corrected hardness ratio, we applied the program *BEHR* by Park et al. (2006).

During most observations, the *Swift* UV-Optical Telescope (UVOT, Roming et al. 2005) observed in all six photometric filters UVW2 (1928 Å), UVM2 (2246 Å), UVW1 (2600 Å), u (3465 Å), b (4392 Å), and v (5468 Å). Before we analyzed the data, all snapshots in one segment were combined with the UVOT tool *uvotimsum*. The flux densities and magnitudes in each filter were determined by the tool *uvotsource* using the count rate conversion and calibration, as described in Poole et al. (2008) and Breeveld et al. (2010). Source counts were extracted in a circle with a radius of  $3''$  and background counts in a nearby source-free region with a radius of  $20''$ . The smaller source extraction radius of  $3''$  was corrected for by setting the UVOT task *uvotsource* parameter *apercorr* = *curveofgrowth*. The UVOT fluxes listed in Table A.2 are not corrected for Galactic reddening. The reddening value in the direction of IRAS 23226-3843 is  $E_{B-V} = 0.025$ , deduced from the Schlafly & Finkbeiner (2011) recalibration of the Schlegel et al. (1998) infrared-based dust map. Applying Eq. (2) in Roming et al. (2005), who used the standard reddening correction curves by Cardelli et al. (1989), we calculated the following magnitude corrections:  $v_{\text{corr}} = 0.083$ ,  $b_{\text{corr}} = 0.109$ ,  $u_{\text{corr}} = 0.136$ ,  $UVW1_{\text{corr}} = 0.177$ ,  $UVM2_{\text{corr}} = 0.244$ , and  $UVW2_{\text{corr}} = 0.205$ . For all *Swift* UVOT magnitudes used in this publication, we adopted the Vega magnitude system.

### 2.2. X-ray observations with XMM-Newton and NuSTAR

The XMM-Newton and NuSTAR observations were taken as part of a ToO program (Proposal ID 08205301, PI Schartel)

aimed at catching AGN in deep minimum or maximum states (see, e.g., Parker et al. 2016, 2019). The observing program consisted of one initial XMM-Newton snapshot, a follow-up long XMM-Newton/NuSTAR exposure, and a final follow-up snapshot with XMM-Newton. The details of these observations are given in Table 1.

We reduced the XMM-Newton data using the XMM-Newton Science Analysis Software (SAS) version 16.1.0. We extracted EPIC-pn and EPIC-MOS spectra for each observation using the *epproc* and *emproc* tools, and filtered for background flares. We took source photons from 30'' circular regions centered on the source position and background photons from large circular regions on the same chip where possible and avoided contaminating sources and the high copper background region of the pn. There was almost no variability during the observations, therefore we focused on analyzing the spectra.

The three XMM-Newton spectra are very similar. Preliminary fitting of the spectra with a power law showed that the spectral indices of the observations are constant, the residuals do not change between observations, and there is only a mild difference in normalization. Because the two short observations do not show major differences and the signal-to-noise ratio (S/N) is too low to reveal smaller changes, we combined the spectra from the three observations into a single spectrum for the remainder of this work. We also combined the spectra from MOS1 and MOS2 into a single combined MOS spectrum.

We reduced the NuSTAR data using the NuSTAR Data Analysis Software (NuSTARDAS) version 1.8.0, and extracted source photons from a 30'' circular region centered on the source position. We extracted background photons from a larger 80'' circular region on the same chip and avoided contaminating sources.

We binned all spectra to an S/N of 6, and to oversample the spectral resolution by a factor of 3. We fit the X-ray spectra in XSPEC version 12.9.1p.

### 2.3. Optical spectroscopy with the SALT telescope

An early optical spectrum of IRAS 23226-3843 was taken with the 4m Blanco telescope at the Cerro Tololo Inter-American Observatory in Chile on 1999 June 21 under nonphotometric conditions (Grupe et al. 2004)<sup>1</sup>. The R-C spectrograph was attached to the telescope, and a slit width of 2'' was used oriented in east-west direction.

We took a new optical spectrum of IRAS 23226-3843 with the 10m Southern African Large Telescope (SALT) after the detection of the X-ray variability on 2017 May 10. A second optical spectrum was secured simultaneously to the deep X-ray observation of XMM-Newton on 2017 June 12. The log of our optical spectroscopic observations with SALT is given in Table 2.

The spectroscopic observations with the SALT telescope were taken under identical instrumental conditions with the Robert Stobie Spectrograph using the PG0900 grating. The slit width was fixed to 2''0 projected onto the sky at an optimized position angle to minimize differential refraction. The spectra were taken with an exposure time of 15 minutes (see Table 2). Seeing full width at half maximum (FWHM) values were 1.5 to 2''.

We covered the wavelength range from 4330 to 7376 Å at a spectral resolution of 6.5 Å. The observed wavelength range corresponds to a wavelength range from 4180 to 7120 Å in the rest frame of the galaxy. There are two gaps in the spectrum caused

by the gaps between the three CCDs: one between the blue and the central CCD chip, and one between the central and red CCD chip covering the wavelength ranges 5347–5416 Å and 6386–6454 Å (5162–5228 Å and 6165–6230 Å in the rest frame). All spectra were wavelength corrected to the rest frame of the galaxy ( $z = 0.0359$ ).

In addition to the galaxy spectra, we also observed necessary flat-field and ThAr and Xe arc frames, as well as spectrophotometric standard stars for flux calibration (LTT1020). The spatial resolution per binned pixel was 0''.2534 for our SALT spectra. We extracted nine columns from our object spectrum, corresponding to 2''.28. The reduction of the spectra (bias subtraction, cosmic-ray correction, flat-field correction, 2D wavelength calibration, night sky subtraction, and flux calibration) was made in a homogeneous way with IRAF reduction packages (e.g., Kollatschny et al. 2001). We obtained S/N values higher than 50 in the continuum.

Great care was taken to ensure high-quality intensity and wavelength calibrations to keep the intrinsic measurement errors very low, as described in Kollatschny et al. (2001, 2003, 2010). The AGN spectra (and our calibration star spectra) were not always taken under photometric conditions. Therefore we calibrated the spectra to the same absolute [O III]  $\lambda 5007$  flux of  $1.01 \times 10^{-14} \text{ erg s}^{-1} \text{ cm}^{-2}$  ( $9.27 \times 10^{-15} \text{ erg s}^{-1} \text{ cm}^{-2}$  in rest frame) taken on 2017 May 10 under clear conditions. The flux of the narrow emission line [O III]  $\lambda 5007$  is considered to be constant on timescales of many years.

## 3. Results

### 3.1. X-ray, UV, and optical continuum variations

*Swift* 0.3–10 keV, UV, and optical light curves for the years 2007 to 2017 are shown in Figures 2 and 3 along with the X-ray count rates and the hardness ratios (see Sect. 2.2). All measurements are listed in Tables A.2 and A.3. The X-ray 0.3–10 keV flux and count rate are clearly variable and decrease by a factor of 35. We also checked whether there is any significant variability in the hardness ratio and photon index  $\Gamma$ . There is no obvious connection with the X-ray flux and count rate variability and the variability of the hardness ratio. The distribution of the hardness ratios is almost Gaussian. Figure 3 shows the X-ray, UV, and optical *Swift* light curves for the detailed campaign in 2017. The UV and optical *Swift* bands closely follow the X-ray light curve. The X-ray light curve exhibits the strongest variability amplitudes. Table 3 gives the variability statistics based on the *Swift* continua (XRT, W2, M2, W1, U, B, and V). We indicate the minimum and maximum fluxes  $F_{\min}$  and  $F_{\max}$ , peak-to-peak amplitudes  $R_{\max} = F_{\max}/F_{\min}$ , the mean flux  $\langle F \rangle$  over the period of observations from JD 54676.78 to 57944.56, the standard deviation  $\sigma_F$ , and the fractional variation

$$F_{\text{var}} = \frac{\sqrt{\sigma_F^2 - \Delta^2}}{\langle F \rangle},$$

as defined by Rodríguez-Pascual et al. (1997). The quantity  $\Delta^2$  is the mean square value of the uncertainties  $\Delta_i$  associated with the fluxes  $F_i$ . The  $F_{\text{var}}$  uncertainties are defined in Edelson et al. (2002). The peak-to-peak amplitude and the fractional variation decrease as a function of wavelength.

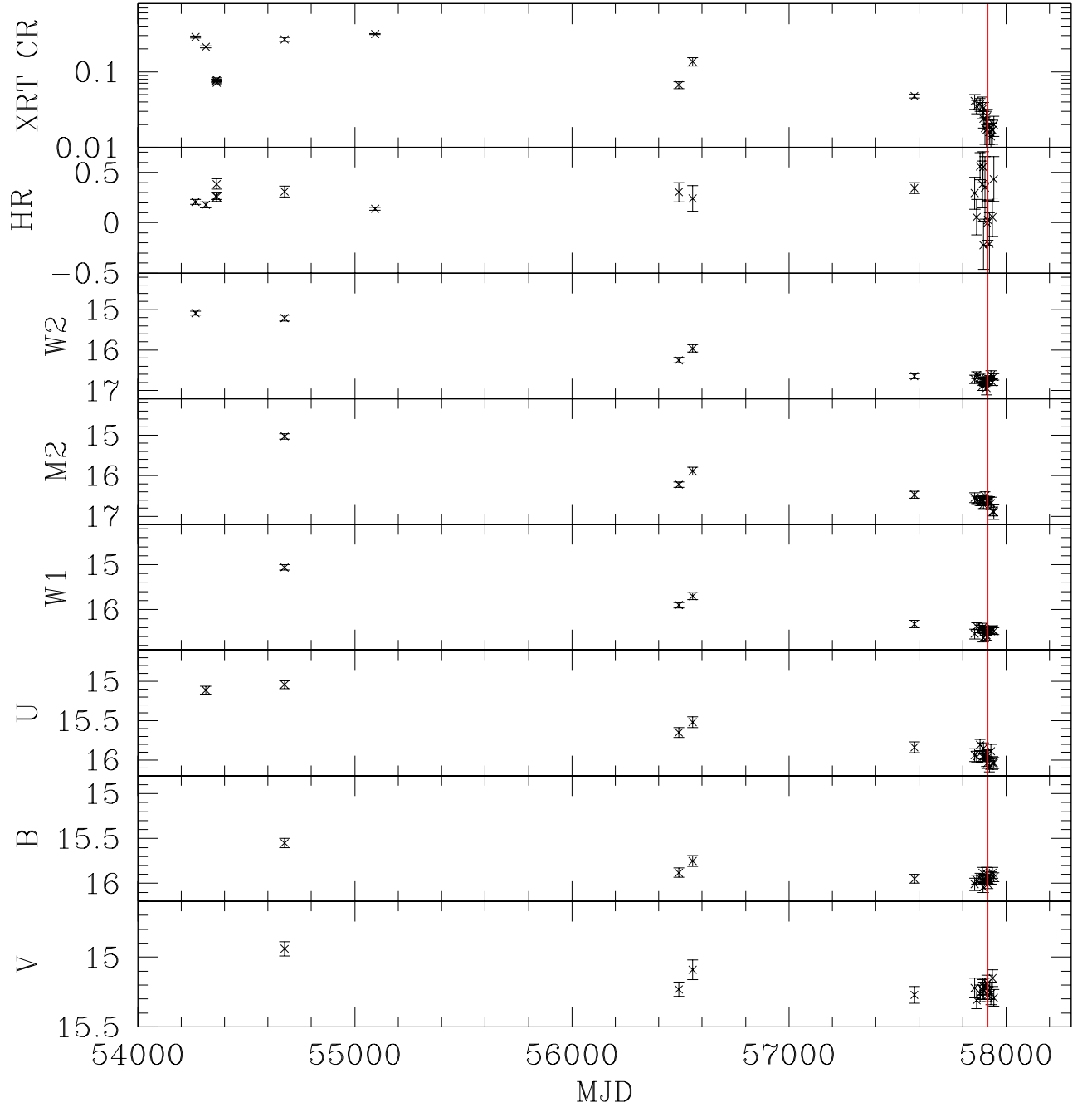
### 3.2. X-ray spectrum

The broadband XMM-Newton/NuSTAR spectrum shows a soft excess, a weak narrow Fe line at 6.4 keV, and a possible ab-

<sup>1</sup> The optical spectrum of IRAS 23226-3843 presented in that paper has erroneously been mixed up.

**Table 1.** Details of the XMM-Newton and NuSTAR X-ray observations. Exposure times are the final clean exposures after filtering for background flares.

Mission	Obs. ID	Julian date 2 400 000+	Start date	Exp. time [ks]
XMM-Newton	0760020101	57875	2017-05-02	12
XMM-Newton	0760020401	57915	2017-06-11	76
NuSTAR	80101001002	57915	2017-06-11	96
XMM-Newton	0760020501	58071	2017-11-14	9

**Fig. 2.** Combined X-ray, UV, and optical light curves taken with the *Swift* satellite for the years 2007 until 2017. The red line indicates the date of our deep XMM-Newton observation on 2017-06-11.

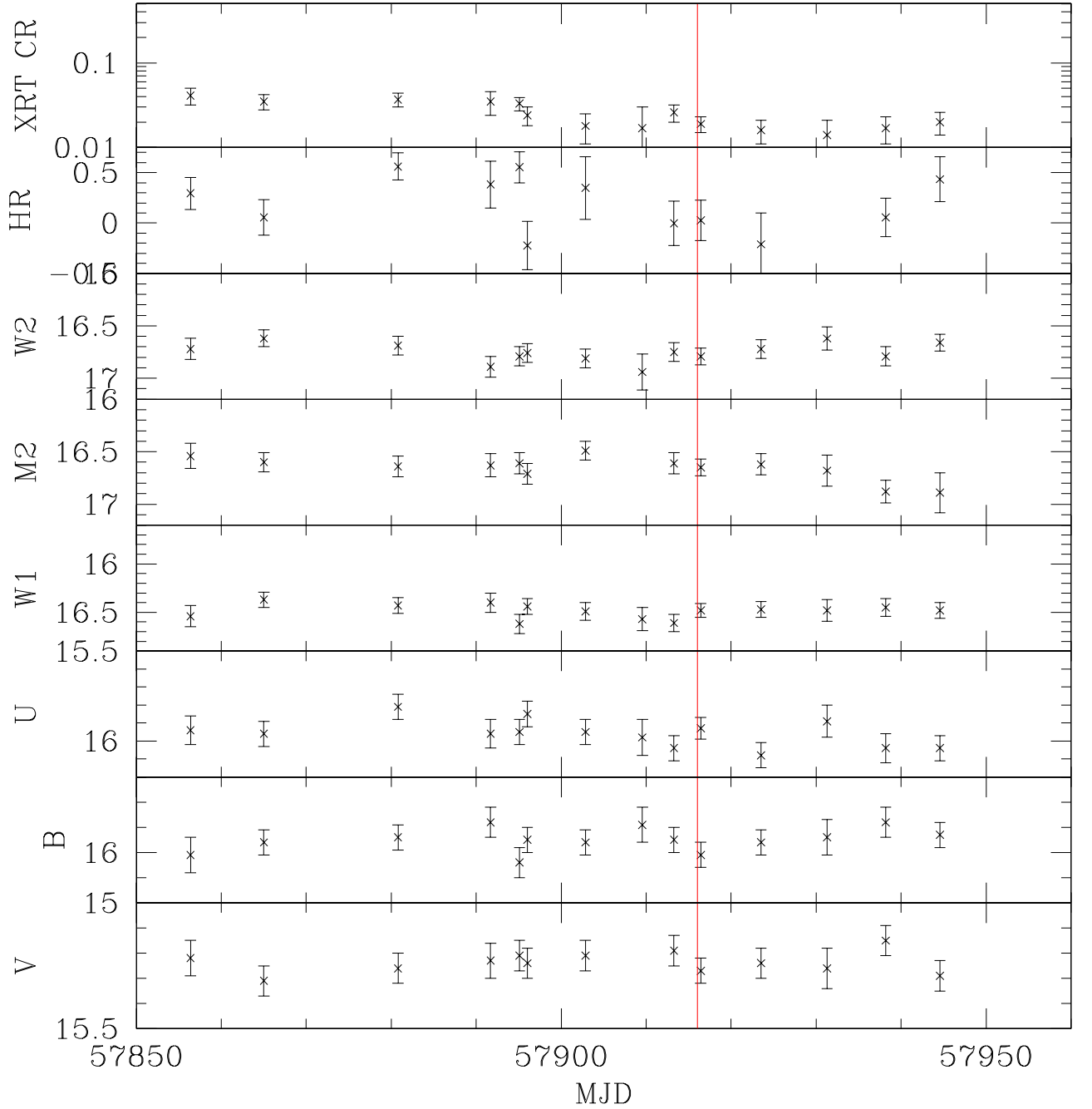


**Fig. 3.** Combined X-ray, UV, and optical light curves taken with the *Swift* satellite for the year 2017. The red line indicates the date of our deep XMM-Newton observation on 2017-06-11.

sorption feature just above 7 keV. We fit the spectrum with Galactic absorption (modeled with TBnew; Wilms et al., 2000), a cut-off power-law continuum, a phenomenological blackbody soft excess, neutral reflection modeled with *xillver* (Garcia et al., 2013) a warm absorber modeled with *xstar* (Kallman & Bautista, 2001), and a Gaussian absorption line. We also allowed for a constant offset between the different detectors to allow for calibration differences and the nonsimultaneous XMM-Newton/NuSTAR exposures. The difference between XMM-Newton and NuSTAR is relatively large because EPIC includes

the two shorter intervals when NuSTAR was not observing. The data are shown in Fig. 4, the best-fit model is shown in Fig. 5, and the parameters are given in Table 4.

This model gives a good fit to the data, with no obvious structured residuals. The significance of the 7.3 keV line is low: although a residual feature is present in all three instruments, it is weak, and the difference in  $\chi^2$  is only 7 for two additional degrees of freedom. If this were real, it would correspond to an outflow with a velocity of  $\sim 0.05c$ , assuming the line is produced

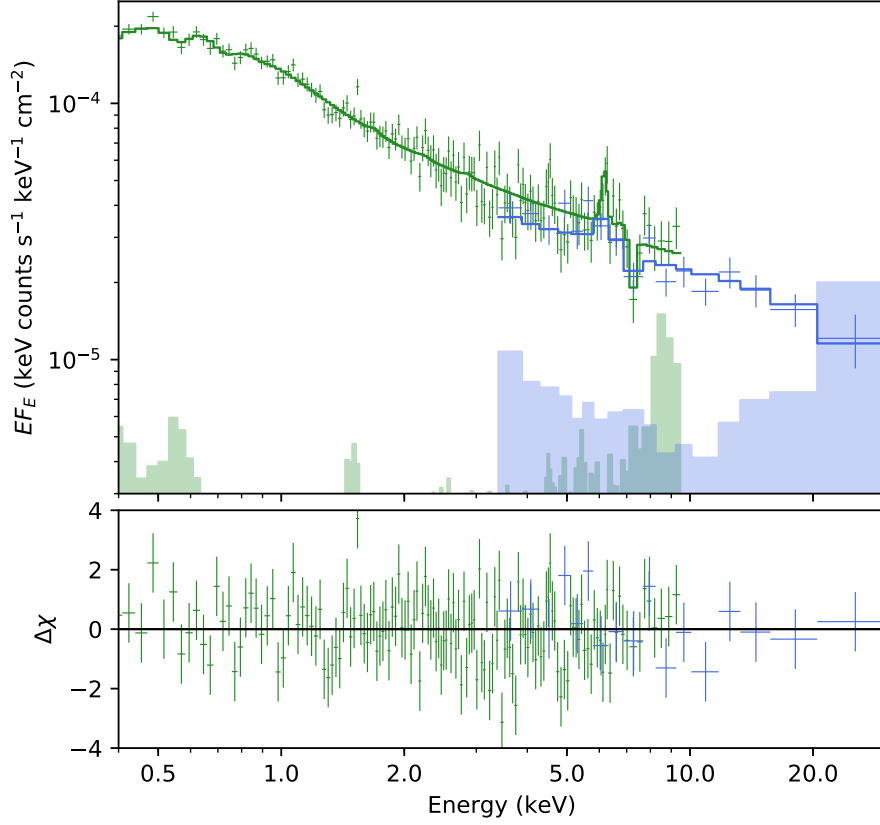


**Fig. 4.** XMM-Newton and NuSTAR spectrum of IRAS 23226-3843. The data are corrected for the effective area of the instruments (using the ‘setplot area’ command in `xspec`) but are not unfolded. Solid lines show the best-fit model, and shaded regions show the background spectra. The lower panel shows the residuals to the best-fit model. For clarity, we show only the EPIC-pn and NuSTAR data. The two NuSTAR FPM spectra are grouped for clarity in the figure, but fitted separately.

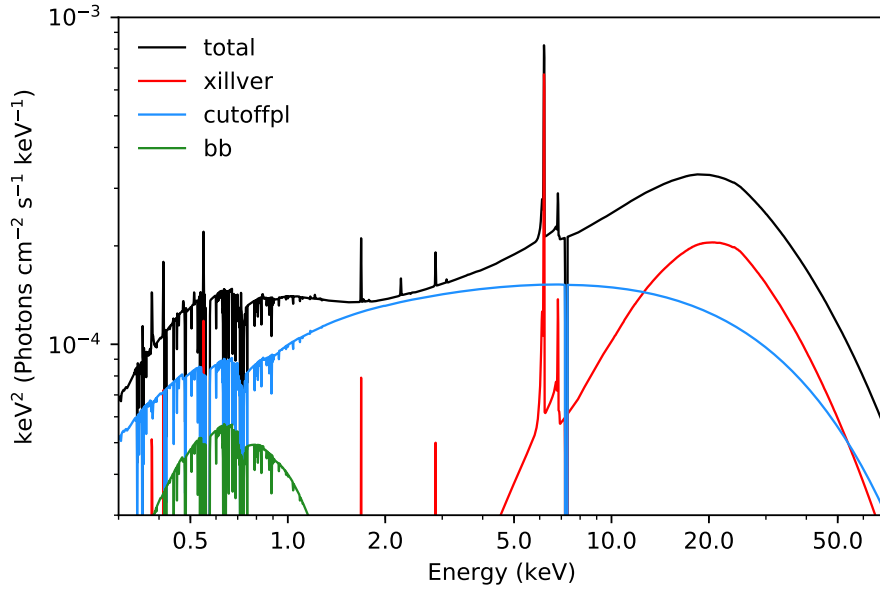


**Fig. 5.** Best-fitting broadband spectral model, showing the different spectral components.

by Fe xxvi, but we cannot claim a detection based on the current data.

### 3.3. Optical spectra and their variations

We show in Figure 6 the optical spectra of IRAS 23226-3843 that were taken with the SALT telescope in May and June 2017. In addition, we present for comparison the optical spectrum

**Table 2.** Log of spectroscopic observations of IRAS 23226-3843 at the Cerro Tololo Inter-American Observatory in 1999 and with the SALT telescope in 2017. Listed are the Julian date, the UT date, and the exposure time.

Julian date 2 400 000+	UT date	Exp. time [s]	comments
51350	1999-06-21	600	clouds
57883	2017-05-10	900	clear, 1'5
57916	2017-06-12	900	clear, 2'0

**Table 3.** Variability statistics based on the *Swift* continua (XRT, W2, M2, W1, U, B, V) in units of  $10^{-12}$  erg s $^{-1}$  cm $^{-2}$  Å $^{-1}$  and  $10^{-12}$  ergs s $^{-1}$  cm $^{-2}$  for the 0.3–10 keV X-ray data.

	F <sub>max</sub>	F <sub>min</sub>	R <sub>max</sub>	<F>	σ <sub>F</sub>	F <sub>var</sub>
XRT	11.45	0.33	34.70	2.03	2.56	1.25 ± 0.62
W2	8.45	1.94	4.36	2.65	2.91	1.10 ± 0.41
M2	10.14	1.84	5.51	3.02	2.07	0.68 ± 0.23
W1	9.79	2.34	4.18	3.39	1.87	0.54 ± 0.16
U	11.74	4.59	2.56	5.75	1.71	0.29 ± 0.05
B	17.18	10.87	1.58	12.30	1.48	0.11 ± 0.01
V	21.59	15.4	1.40	16.85	1.41	0.06 ± 0.005

**Table 4.** Best-fit model parameters for the broadband X-ray spectrum. Normalization constants are defined relative to the EPIC-pn normalization.

Parameter	Value	Description
$E_{\text{Gauss}}$	$7.34^{+0.07}_{-0.12}$	Gaussian energy (keV)
$N_{\text{H}}$	$(4 \pm 2) \times 10^{20}$	Column density (cm $^{-2}$ )
$\log(\xi)$	$0.6^{+0.3}_{-0.5}$	Ionization (erg cm s $^{-1}$ )
$\Gamma$	$1.75^{+0.03}_{-0.04}$	Photon index
$E_{\text{cut}}$	$30^{+20}_{-10}$	Cut-off energy (keV)
$A_{\text{Fe}}$	$< 0.8$	Iron abundance
$kT$	$0.17 \pm 0.01$	Blackbody temperature (keV)
$C_{\text{pn}}$	1*	EPIC-pn constant
$C_{\text{MOS}}$	$1.09 \pm 0.01$	EPIC-MOS constant
$C_{\text{FPMA}}$	$0.84 \pm 0.05$	FPMA constant
$C_{\text{FPMB}}$	$0.82 \pm 0.05$	FPMB constant
$\chi^2/\text{dof}$	421/395	Fit statistic

taken with the 4m Blanco telescope at the Cerro Tololo Observatory on 1999 June 21 (Grupe et al. 2004). Furthermore, we show the difference spectrum between 1999 and May 2017 when IRAS 23226-3843 was in a minimum state. The original optical spectra were taken with different telescopes and different spectrographs and also under different atmospheric conditions. Therefore we had to intercalibrate our spectra. The intercalibration of the spectra in Figure 6 was carried out with respect to the [O III]  $\lambda$ 5007 line as well as with respect to the narrow H $\alpha$ , [NII], and [SII] lines next to H $\alpha$  because the flux of the narrow emission lines is considered to be constant on timescales of years. Because the spectrum of IRAS 23226-3843 shows a strong additional contribution from the underlying host galaxy and the narrow emission line region is extended, a relative flux accuracy of only about 5% was achieved for the nuclear emission line spectra.

The spectrum taken in 1999 exhibits an asymmetric broad H $\alpha$  emission, a broad double-peaked H $\beta$  emission, and permitted broad FeII blends of the multiplets 37 and 38 and 42, 48, 49. These broad H $\alpha$  and H $\beta$  lines as well as FeII blends are variable, as can be seen in the difference spectrum between 1999 and 2017

**Table 5.** Wavelength ranges of the (pseudo-) continua, the Balmer lines, and FeII blends.

Continuum, Line	Wavelength range [Å]
Cont 4385	4375 – 4390
Cont 5085	5060 – 5110
Cont 5640	5620 – 5660
Cont 6120	6095 – 6145
Cont 6880	6870 – 6890
FeII(37,38)	4390 – 4700
H $\beta$ <sub>broad</sub>	4700 – 5050
FeII(42,48,49)	5110 – 5600
H $\alpha$ <sub>broad</sub>	6260 – 6870

**Table 6.** Optical emission line fluxes in IRAS 23226-3843 and line fluxes relative to H $\beta$  in 1999.

Line	Flux	Relative Fluxes
[OIII]4363	23.3±2.	0.038
FeII(37,38)	467.3 ± 30.	0.78
H $\beta$ <sub>broad</sub>	600.7±25.	1.
[OIII]4959	27.9±2.	0.046
[OIII]5007	92.7±3.	0.15
FeII(42,48,49)	362.0±30.	0.60
[FeVII]5721	13.2±1.	0.022
[FeX]6375	9.3±1.	0.015
[NII]6548	12.9±1.	0.021
H $\alpha$ <sub>narrow</sub>	44.7±2.	0.074
H $\alpha$ <sub>broad</sub>	1192.6±40.	1.98
[NII]6584	53.1±2.	0.088
[SII]6717	12.5±1.	0.021
[SII]6731	16.1±1.	0.027

**Notes.** Line fluxes in units  $10^{-16}$  erg s $^{-1}$  cm $^{-2}$ 

(see the bottom spectrum in Figure 6). In addition to the broad lines, the typical narrow AGN emission lines of [OIII], [OII], [NII], [SII], a narrow H $\alpha$ , and the coronal lines [FeVII]5721 and [FeX]6375 are present. The contribution of the host galaxy spectrum is strong in this AGN based on its overall spectral behavior and on the strong stellar absorption features.

The wavelength ranges of the continua and pseudo-continua we used for the broad Balmer lines and FeII blends are given in Table 5. The pseudo-continua were used to subtract a continuum below the variable broad emission lines. We present in Table 6 the rest frame emission-line intensities based on the spectrum taken in 1999. We corrected the derived FeII( $\lambda$ 5110–5600Å) flux for the Mgb absorption. Furthermore, we list in Table 7 the broad-line fluxes of H $\alpha$ , H $\beta$ , and of the FeII blends (37 and 38) and (42, 48, and 49) for the three observing epochs in 1999 and 2017. In addition, we present the observed continuum flux at 5085±25Å as well as the continuum flux after subtraction of the host galaxy continuum flux of  $9.19 \times 10^{-16}$  erg s $^{-1}$  cm $^{-2}$  Å $^{-1}$ . We also give the continuum and line flux ratios with respect to the spectrum taken in 1999.

The host galaxy contribution in the optical spectra of IRAS 23226-3843 is strong, as has been reported before. Based on the spectrum taken in May 2017, we derived a mean host galaxy spectrum by extracting a spectrum between 1.9'' and 3.2'' on both sides of the nucleus. This mean host galaxy spectrum is free of broad Balmer lines and FeII blends. The spectra of the central region (AGN + host galaxy), of the host galaxy,

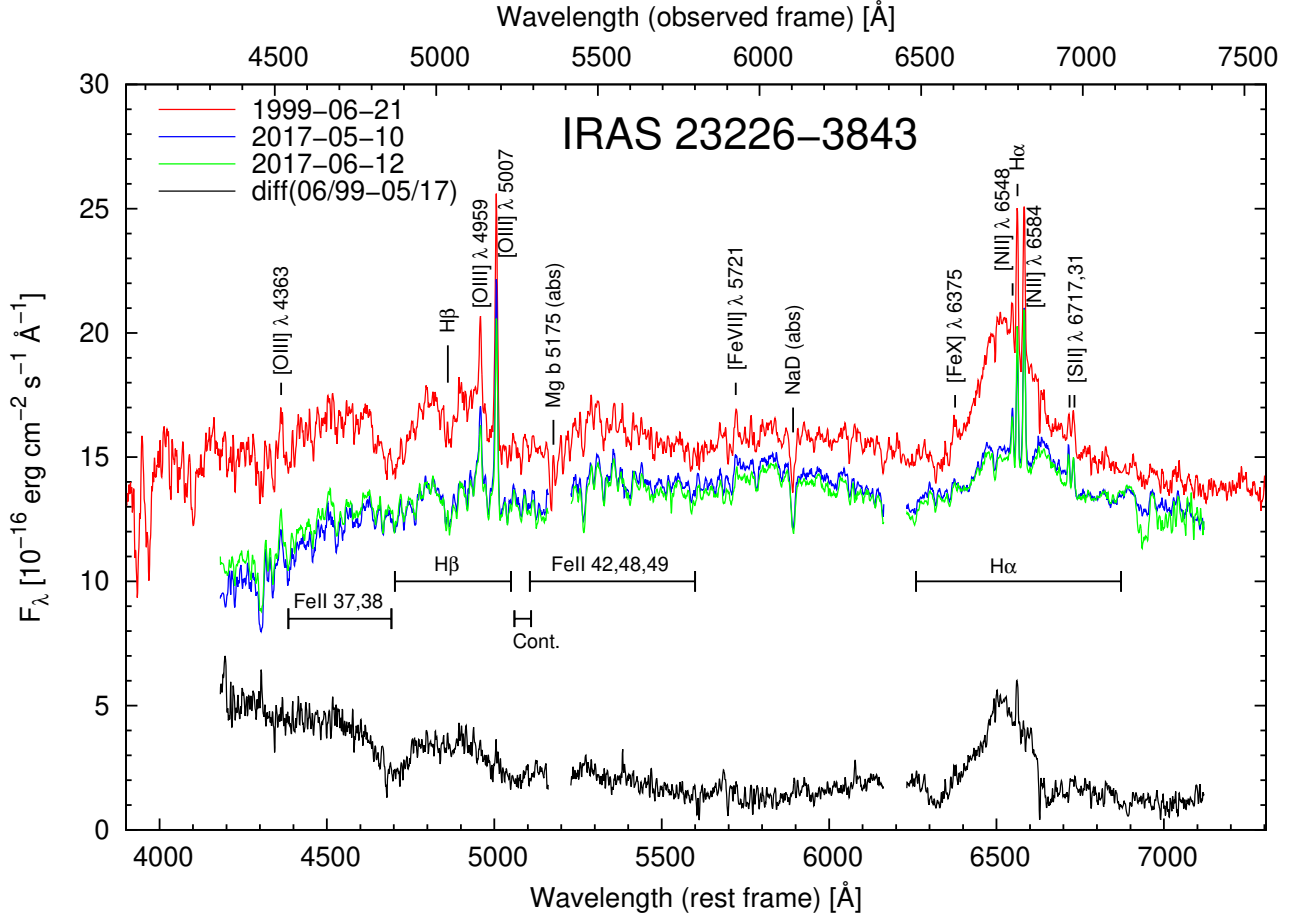


**Fig. 6.** Optical spectra of IRAS 23226-3843 taken in 2017 as well as in 1999. The spectrum at the bottom gives the difference between the spectra taken in 1999 and May, 2017.

**Table 7.** Intensities of the optical continuum and of the integrated broad lines with their relative variations.

date	Cont	Cont <sub>w.o.host</sub>	FeII(37,39)	H $\beta$ <sub>broad</sub>	FeII(42,48,49)	H $\alpha$ <sub>broad</sub>
1999-6	15.27 $\pm$ 0.4	6.08 $\pm$ 0.4	467. $\pm$ 30.	601. $\pm$ 25.	362. $\pm$ 30.	1193. $\pm$ 40.
2017-5	13.19 $\pm$ 0.3	4.00 $\pm$ 0.3	360. $\pm$ 30.	316. $\pm$ 25.	316. $\pm$ 30.	629. $\pm$ 30.
2017-6	12.94 $\pm$ 0.3	3.75 $\pm$ 0.3	391. $\pm$ 30.	338. $\pm$ 25.	339. $\pm$ 30.	570. $\pm$ 30.
99/17-5	1.16	1.52	1.30	1.90	1.15	1.90
99/17-6	1.18	1.62	1.19	1.78	1.07	2.09

**Notes.** Continuum flux in units of  $10^{-16} \text{ erg s}^{-1} \text{ cm}^{-2} \text{ \AA}^{-1}$ ,  
Line fluxes in units  $10^{-16} \text{ erg s}^{-1} \text{ cm}^{-2}$ .

and of the clean AGN spectrum after subtraction and correction for the underlying host galaxy component are shown in Figure 7. We scaled the host galaxy spectrum in such a way that the stellar absorption features were minimized in the nuclear difference spectrum. Finally, we subtracted the scaled host galaxy spectrum from the nuclear spectrum. The final difference spectrum is composed of the central nonthermal component, the broad emission lines, and some narrow [OIII] emission line residuals. These narrow emission lines originate not only in the nucleus, but also come from off-nuclear regions probably as a result of starbursts and/or shock heating.

The variations of the optical continua and of the integrated broad lines are shown in Figure 6 and Table 7. In addition, we present the continuum and line flux ratio of the observa-

tions in 1999 (high state) with respect to the fluxes in 2017 (low state) in Table 7. The clean continuum after subtraction of the host galaxy component was fainter by a factor of 1.5 in 2017 than in 1999. The broad H $\alpha$  and H $\beta$  emission lines fluxes decreased by a factor of 1.9 and the FeII blends only decreased by a factor of 1.2. The continuum and Balmer line fluxes of the spectra from May and June 2017 are identical to within 5%. The equivalent width (EW) of the [OIII] $\lambda$ 5007 line amounts to  $14.6 \pm 2. \text{ \AA}$  ( $\log[\text{OIII}]=1.16 \pm 0.05$ ) in 1999 and to  $18.8 \pm 2. \text{ \AA}$  ( $\log[\text{OIII}]=1.27 \pm 0.05$ ) in 2017 after correction for the host galaxy contribution.



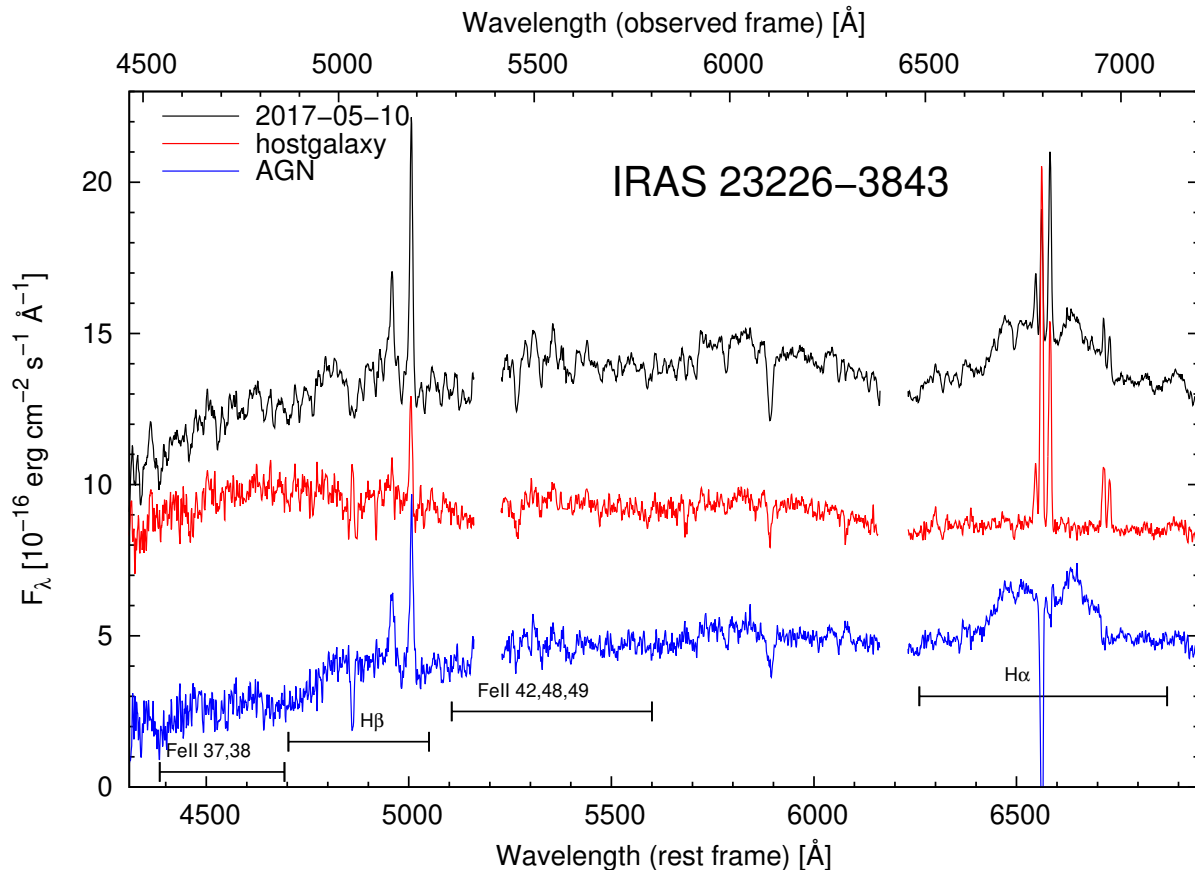


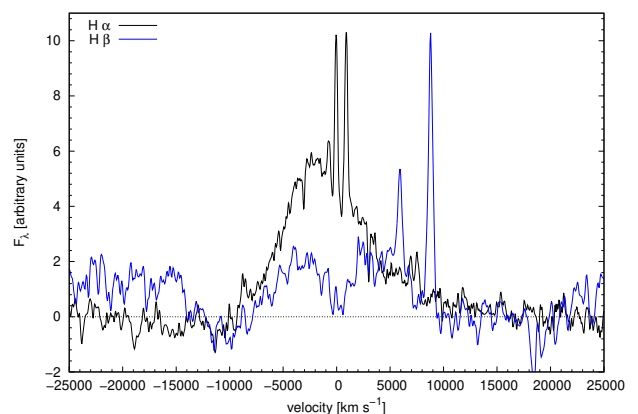
**Fig. 7.** Central optical spectrum of IRAS 23226-3843 and a spectrum of the host galaxy (June 2017). The spectrum at the bottom gives the broad lines and the nonthermal continuum component after subtraction of the host galaxy spectrum.

### 3.3.1. Balmer emission line profiles and their variations

Based on the spectra presented in Figs. 6 and 7, it is evident that the Balmer lines in IRAS 23226-3843 are very broad. We present in Table 8 the line width FWHM and the full width at zero intensity (FWZI) of  $H\alpha$  and  $H\beta$ . The FWHM of  $H\beta$  and  $H\alpha$  amounts to  $\sim 12\,000\text{ km s}^{-1}$  in all spectra, except for the  $H\alpha$  profile in 1999, which showed a strong asymmetry. The FWZI in all spectra amounts to  $\sim 19\,000\text{ km s}^{-1}$ .

We present in Figure 8 a comparison of the  $H\alpha$  and  $H\beta$  line profiles in velocity space after subtraction of the underlying continua for the spectrum taken in 1999. The comparison of the  $H\alpha$  and  $H\beta$  line profiles shows considerable differences between the profiles. The  $H\alpha$  profile is asymmetric with respect to  $v=0\text{ km s}^{-1}$ . More specifically, the center of the broad component is blueshifted by  $-1\,880\text{ km s}^{-1}$  with respect to the narrow  $H\alpha$  component. The  $H\beta$  profile, however, is symmetric with respect to  $v=0\text{ km s}^{-1}$  and shows a double-peaked profile. It is evident that in the high state, the Balmer decrement  $H\alpha/H\beta$  is different for the red and blue wings.

We present in Figure 9 a comparison of the  $H\alpha$  and  $H\beta$  line profiles in velocity space for May 2017, when IRAS 23226-3843 was in the low state. As mentioned before, we first subtracted a spectrum of the host galaxy as seen in Figure 7 because the relative contribution of the host galaxy is very strong. The subtraction of the host galaxy spectrum leads to a central absorption in  $H\alpha$  and  $H\beta$  because the Balmer emission is extended in

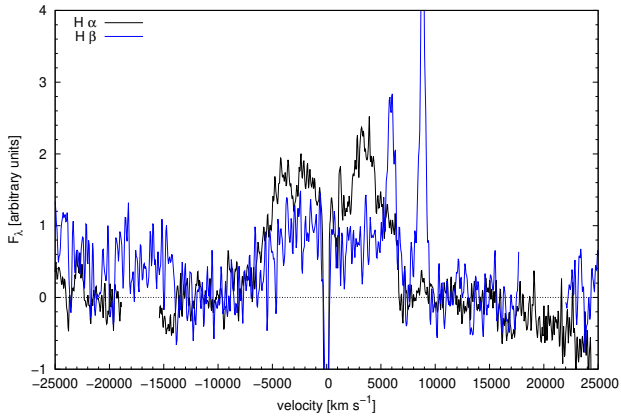


**Fig. 8.** Line profiles of  $H\alpha$  and  $H\beta$  (for 1999) in velocity space after subtraction of the host galaxy spectrum.

IRAS 23226-3843. During the low state, the profiles of both the broad  $H\alpha$  and  $H\beta$  line are symmetric. Their double-peaked shape is typical for an underlying accretion disk. The line profile variations in the red and blue wings of  $H\alpha$  and  $H\beta$  differ from 1999

**Table 8.** Balmer line width FWHM and FWZI (left wing, right wing, total) in units of  $\text{km s}^{-1}$  for 1999 and May 2017

line (date)	FWHM(left)	FWHM(right)	FWHM	FWZI(left)	FWZI(right)	FWZI
H $\beta$ (99)	-6120 $\pm$ 200	6960 $\pm$ 200	13080 $\pm$ 300	-9770 $\pm$ 500	9720 $\pm$ 500	19500 $\pm$ 700
H $\alpha$ (99)	-5200 $\pm$ 500	3150 $\pm$ 500	8360 $\pm$ 700	-9780 $\pm$ 500	10650 $\pm$ 500	20430 $\pm$ 700
H $\beta$ (17)	-5490 $\pm$ 200	6930 $\pm$ 200	12420 $\pm$ 300	-8550 $\pm$ 800	9800 $\pm$ 500	18350 $\pm$ 1000
H $\alpha$ (17)	-5150 $\pm$ 200	5920 $\pm$ 200	11060 $\pm$ 300	-9340 $\pm$ 800	8400 $\pm$ 800	17740 $\pm$ 1000

**Fig. 9.** Line profiles of H $\alpha$  and H $\beta$  (for May 2017) in velocity space after subtraction of the host galaxy spectrum.

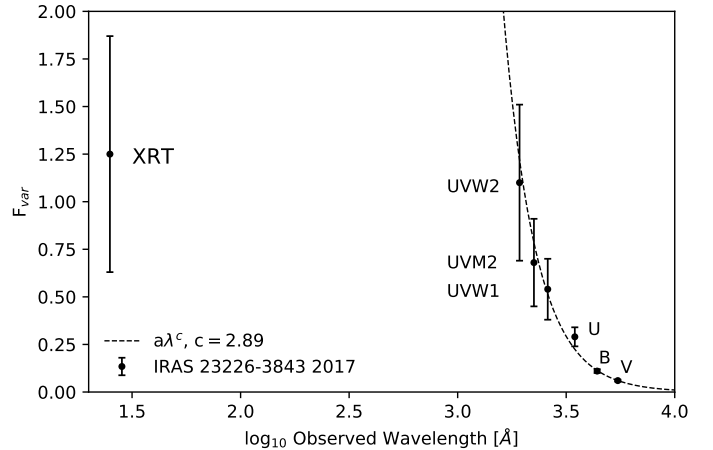
to 2017: H $\alpha$  shows considerably stronger variations in the blue wing than in the red wing. The Balmer decrement (1.8 – 2.0) is quite low and different for 1999 and 2017.

## 4. Discussion

### 4.1. X-ray, UV, and optical continuum variations

The X-ray, UV, and optical continuum light curves of IRAS 23226-3843 show the same variability trend from 2007 to 2017 (Figures 2 and 3). The decreasing trend during 2017 was strongest in the X-rays and less pronounced in the optical B and V bands (Fig. 3). IRAS 23226-3843 decreased in the X-rays by a factor of more than 30 from 2007 until 2017 (Swift, ROSAT). The variability amplitudes become systematically smaller from the X-ray to the optical *Swift* bands from a factor of 35 to a factor of about 2 (see Table 3). The U, B, V *Swift* bands were not corrected for the contribution of the host galaxy. The broad H $\alpha$  line flux also decreased by a factor of 2 from 1999 until 2017.

The fractional variation  $F_{\text{var}}$  is another way to describe the variability strength in AGN. We present the fractional variation of the X-ray band together with the fractional variations of the UV and optical bands in Table 3 and Figure 10. The fractional variations are stronger at shorter wavelengths. Interestingly, the fractional variation in X-rays does not follow the same trend as the fractional variations in the UV and optical bands, and the extrapolation of the fit in the UV and optical bands does not agree with the X-ray observations. This is an indication that the origin of the UV/optical emission is not a simple extension of the origin of the X-ray continuum emission. A similar behavior has been found in the changing-look AGN HE 1136-2304 (Zetzl et al. 2018). The prototype AGN NGC 5548 shows an even lower

**Fig. 10.** Fractional variations of the X-ray, UV, and optical continuum bands measured from the *Swift* data as a function of wavelength.

correlation of the X-rays with the UV/optical continuum (Edelson et al. 2015).

We now compare the fractional variations in the UV and optical bands in IRAS 23226-3843 with those of the variability campaigns in HE 1136-2304 and NGC 5548 (Zetzl et al. 2018, Edelson et al. 2015, Fausnaugh et al. 2016): The fractional variations in the UV and optical bands in the changing-look HE 1136-2304 were stronger by a factor of 2.3 than in NGC 5548. The fractional variations in our present study of IRAS 23226-3843 are even stronger by a factor of 2 than those in HE 1136-2304, indicating the extreme flux variations in IRAS 23226-3843.

### 4.2. X-ray spectrum

The broadband XMM-Newton/NuSTAR spectrum is power-law dominated with a contribution from photoionized emission from cold gas, likely the outer accretion disk or torus. The fit is improved when a small amount of warm absorption at low energies is included, but this is not clearly resolved by the EPIC instruments and therefore might instead be due to a more complex continuum or soft excess. The RGS data do not have enough signal to determine how much absorption is present because the source flux is low.

There is a possible weak absorption line at  $\sim 7.3$  keV, with a residual feature in both XMM-Newton and NuSTAR spectra. If this were genuine, it would indicate a mildly relativistic outflow, with a velocity of  $0.05c$ . However, this feature is not statistically significant ( $\sim 2\sigma$ ), therefore we cannot claim a detection. The spectrum shows no evidence for a significant column of neutral absorption, which can cause X-ray low states in some sources (e.g., Parker et al. 2014), or a relativistic reflection component, which can dominate when the primary continuum drops strongly (e.g., Fabian et al. 2012).

### 4.3. Optical spectrum: extremely broad and double-peaked Balmer profiles

IRAS 23226-3843 was classified as Seyfert 1 type (Allen et al. 1991) based on a spectrum taken between 1985 and 1990. It was of clear Seyfert type 1 in 1999 as well (see Figure 6). The broad  $H\alpha$  line profile was asymmetric. The center of the broad  $H\alpha$  component was blueshifted with respect to the narrow emission by  $-1900 \text{ km s}^{-1}$  (see Figure 8). In contrast to this,  $H\beta$  shows a broad symmetric double-peaked emission line profile.

It is generally accepted that broad double-peaked profiles originate in relativistic Keplerian disks of gas surrounding the central supermassive black hole (e.g., Eracleous & Halpern 1994). During the minimum state in 2017, the two Balmer lines ( $H\alpha$  and  $H\beta$ ) show the same symmetric double-peaked profile. The peak separation corresponds to  $7000 \text{ km s}^{-1}$ . The broad Balmer line components, especially of  $H\alpha$ , are faint and barely visible in 2017 in comparison to the optical spectra taken in 1999. IRAS 23226-3843 was of Seyfert type 1.9 during the minimum state in 2017. When the optical spectra taken in May and June 2017 are compared (Figure 6), the broad  $H\alpha$  component was slightly stronger in May 2017.

The Balmer decrement  $H\alpha/H\beta$  had a very low value of lower than 2 in 2017 and only about 2 in 1999 (see Table 7). These values are far below the expected Case B recombination value of 2.7 (Osterbrock & Ferland 2006). The observed unusual flat Balmer decrement in IRAS 23226-3843 indicates a very high hydrogen density of  $n_H > 10^{11} \text{ cm}^{-3}$  to the center of the accretion disk (see the discussion of intrinsic hydrogen-line ratios in Gaskell, 2017).

The asymmetry of  $H\alpha$  during the maximum state in 1999 might have been caused by absorption of the red component. Partial dust obscuration of the BLR by outflowing dust clumps, a model introduced by Gaskell & Harrington (2018), can produce asymmetries and velocity-dependent lags. However, the derived Balmer decrement in IRAS 23226-3843 is far below the Case B value of 2.7 and therefore does not indicate extinction. The X-ray spectrum was unabsorbed as well during the minimum state. The observed low  $H\alpha/H\beta$  ratios in the emission line wings are rather an indicator for high densities in the innermost clouds. It was previously discovered by Shuder (1982), for instance, that the Balmer decrement is flatter in the outer emission line wings that originate closer to the center. During the high state of IRAS 23226-3843 in 1999, other cloud regions might have been ionized than in the conditions in 2017.

There are clear signs for an additional blue absorption component in the  $H\alpha$  and  $H\beta$  line profiles at  $v = -11\,000 \text{ km s}^{-1}$  (Figures 6 and 8). Intriguingly, there is further evidence for a possible weak absorption line at  $\sim 7.3 \text{ keV}$  in X-rays, indicating a mildly relativistic outflow with  $v = -11\,000 \text{ km s}^{-1}$ . A blue absorption component in the Balmer lines at  $v \sim -11\,000 \text{ km s}^{-1}$  like this has also been detected in another very broad-line AGN (Mrk 926) (Kollatschny 2010), indicating a high-velocity outflow component.

The broad double-peaked Balmer line profiles and their strong variations in IRAS 23226-3843 are similar to those of other broad double-peaked galaxies such as NGC 1097 (Storchi-Bergmann et al. 1997), or broad-line radio galaxies such as 3C390.3 (Shapovalova et al. 2010) and Arp102B (Shapovalova et al. 2013). Strateva et al. (2003) studied the properties of double-peaked Balmer line AGN in a large sample of SDSS galaxies. In comparison to all these double-peaked AGN, IRAS 23226-3843 shows significantly stronger FeII line blends. In general, broad-line AGN are expected to show only weak FeII line blends according to Eigenvector 1 studies of AGN (Boro-

son & Green 1992, Sulentic et al. 2000). The Eigenvector 1 is the dominant trend in AGN in which many properties correlate with the relative strength of optical FeII and [O III] line emission/equivalent widths. Not a single AGN in the sample of about 20,000 SDSS quasars (Shen & Ho 2014, their Fig.1) shows such broad  $H\beta$  line widths of  $12,400 \text{ km s}^{-1}$  (in 2017) or  $13,000 \text{ km s}^{-1}$  (in 1999) in the two-dimensional Eigenvector 1 plane.

We determined relative FeII strengths  $\text{EW(FeII)}/\text{EW(H}\beta\text{)}$  of 0.6 (in 1999) and 1.0 (in 2017) in IRAS 23226-3843. These values agree with the derived [OIII] $\lambda 5007$  equivalent widths of  $14.6 \pm 2. \text{ \AA}$  (1999) and  $18.8 \pm 2. \text{ \AA}$  (2017) in the two-dimensional Eigenvector 1 plane. However, the position of IRAS 23226-3843 is unique in the two-dimensional Eigenvector 1 plane of Shen & Ho 2014 based on its extreme broad Balmer line widths in combination with relative strong FeII emission. One way to explain this discrepancy between IRAS 23226-3843 and the SDSS quasar sample might be the fact that the flat Balmer decrement and therefore the high-density emission line region is unique in IRAS 23226-3843 in comparison to the SDSS quasars (Dong et al. 2008, Gaskell 2017). In addition, IRAS 23226-3843 is only a low-luminosity Seyfert galaxy with a low Eddington ratio in contrast to the more luminous SDSS quasars in the sample of Shen & Ho (2014). In addition, a low Eddington ratio of  $L/L_{\text{edd}} = 0.01$  has been derived before by Grupe et al. (2004) for IRAS 23226-3843 during the high state based on its broad emission lines and therefore high black hole mass of  $M_{\text{BH}} = 1.7 \times 10^8 M_{\odot}$ . The flat X-ray spectral slope  $\alpha_x = 0.60$  (Grupe et al. 2010) is in accordance with a low Eddington ratio in IRAS 23226-3843. Low  $L/L_{\text{edd}}$  supports a disk-wind model for the broad-line region (MacLeod et al. 2019).

### 4.4. Changing-look characteristics in IRAS 23226-3843

The broad-line profiles in IRAS 23226-3843 changed from a Seyfert 1 to a Seyfert 1.9 type during the observing period from 1999 until 2017. The general decrease in the broad-line components and in the optical continuum by a factor of 2.5 from 1999 to 2017 in combination with the change of the Seyfert type is accompanied by a strong decrease of the *Swift* X-ray flux by a factor of 35. These are the characteristics of a changing-look AGN. The spectral type variations followed the continuum intensity variations on timescales of months to years.

A similar spectral type scenario with decreasing continuum flux as seen in IRAS 23226-3843 has been discovered before in Fairall 9. In the case of Fairall 9, the optical continuum flux even dropped to 20% of its original flux level within six years, and the spectral type changed from a quasar/Seyfert 1 type to a Seyfert 1.95 type (Kollatschny & Fricke 1985). More recently, many new cases of changing-look sources have been identified in AGN in single well-studied nearby AGN (e.g., Parker et al. 2019, Oknyansky et al. 2019, Trakhtenbrot et al. 2019, Wang et al. 2019) and in dedicated searches of large databases (e.g., Graham et al. 2020). Spectral variations of the Seyfert type generally occur on timescales of years, such as in the changing-look AGN HE 1136-2304 (Kollatschny et al. 2018, and references therein). The case of IRAS 23226-3843 is special in comparison to HE 1136-2304 and other changing-look AGN because its X-ray drop is extremely high and its Balmer-line profile is exceptionally broad and double-peaked.

A change of the luminosity is always connected with a change of the Eddington ratio  $L/L_{\text{edd}}$  in AGN because the central black hole mass does not change on short timescales.

IRAS 23226-3843 showed a low Eddington ratio of  $L/L_{\text{edd}}=0.01$  in its high state in 1999. The optical luminosity was even lower by a factor of 2.5 for the low state in 2017. The observed low Eddington ratio in IRAS 23226-3843 matches investigations of Noda & Done (2018) and MacLeod et al. (2019), for example. Noda & Done (2018) suggested that all changing-look AGNs are associated with the state transition at Eddington ratios of a few percent. In a similar manner, extreme variable quasars show systematically lower Eddington ratios (Rumbaugh et al. 2018). MacLeod et al. (2019) noted that changing-look quasars are at lower Eddington ratios than the overall quasar population in the SDSS catalog.

Based on the observed long-term light curve, a tidal disruption event or microlensing can be excluded as an explanation for the variability pattern in IRAS 23226-3843. Absorption-based variability is unlikely because the Balmer lines show no indication for large-scale optical extinction and no X-ray absorption could be proved during the minimum state. Various physical scenarios and their timescales to explain the changing-look phenomenon are discussed in Stern et al. (2018), for instance: The relevant timescales for changes at the inner accretion disk surrounding the central black hole are either the thermal or the heating/cooling front timescale. It has been pointed out by Lawrence (2018), for example that the viscous timescale of a viscous radial inflow is too long in comparison to the observed timescales of months to years. Most likely triggers for the observed changes on timescales of years in IRAS 23226-3843 are therefore magnetorotational instabilities (e.g., Ross et al. 2018) or accretion disk instabilities (e.g., Nicastro 2003).

## 5. Summary

We presented results of an optical, UV, and X-ray variability study of IRAS 23226-3843 with XMM-Newton, NuSTAR, *Swift*, and SALT. Our findings are summarized below.

- (1) The optical, UV, and X-ray continuum light curves showed the same variability pattern for 1999 until 2017.
- (2) There were extreme X-ray, UV, and optical variability amplitudes in IRAS 23226-3843. It varied in the X-ray continuum by a factor of 35 and in the optical by a factor of 2.
- (3) The spectral type of IRAS 23226-3843 changed from a clear Seyfert 1 type to a Seyfert 1.9 type, confirming its changing-look AGN character.
- (4) The broadband XMM-Newton/NuSTAR spectrum is power-law dominated, with a contribution from photoionized emission from cold gas, likely the outer accretion disk or torus.
- (5) We did not find evidence that the continuum and line variability (the changing look) is driven by absorption: while there is tentative evidence for a remarkable outflow component at  $v = -11\,000\text{ km s}^{-1}$  seen in absorption, the broadband X-ray spectrum is unabsorbed and the optical broad Balmer lines do not show evidence for extinction. Therefore we favor true changes caused by accretion disk instabilities or magnetorotation instabilities as the driving mechanism behind the changing look.
- (6) In addition to the broad Balmer lines, IRAS 23226-3843 exhibits strong FeII blends, in contrast to what is expected from Eigenvector 1 studies.
- (7) IRAS 23226-3843 shows exceptionally broad and double-peaked Balmer lines. The broad double-peaked profiles originate in a relativistic Keplerian disk of gas surrounding the central supermassive black hole. The unusually low Balmer

decrement  $H\alpha/H\beta$  with a numerical value of two only indicates a very high hydrogen density  $n_H > 10^{11}\text{ cm}^{-3}$  to the center of the accretion disk.

**Acknowledgements.** WK thanks Hartmut Winkler for lively debates on the optical spectra of IRAS 23226-3843. He also thanks Gary Ferland for valuable comments. This paper is based on observations obtained with XMM-Newton, an ESA science mission with instruments and contributions directly funded by ESA Member States and NASA. Based on observations obtained with the Southern African Large Telescope. We thank the *Swift* team for performing the ToO observations. This research has made use of the XRT Data Analysis Software (XRTDAS) developed under the responsibility of the ASI Science Data Center (ASDC), Italy. This research has made use of the NASA/IPAC Extragalactic Database (NED) which is operated by the Jet Propulsion Laboratory, Caltech, under contract with the National Aeronautics and Space Administration. This work made use of data from the NuSTAR mission, a project led by the California Institute of Technology, managed by the Jet Propulsion Laboratory, and funded by the National Aeronautics and Space Administration. This research has made use of the NuSTAR Data Analysis Software (NuSTARDAS) jointly developed by the ASI Science Data Center (ASDC, Italy) and the California Institute of Technology (USA). This work has been supported by the DFG grant Ko 857/33-1.

## References

- Allen, D.A., Norris, R.P., Meadows, V.S. et al. 1991, MNRAS, 248, 528  
 Arnaud, K. A., 1996, ASP Conf. Ser. 101: Astronomical Data Analysis Software and Systems V, 101, 17  
 Boroson, T.A., & Green, R.F. 1992, ApJS, 80, 109  
 Breeveld, A.A., et al. 2010, MNRAS, 406, 1687  
 Burrows, D., et al. 2005, Space Science Reviews, 120, 165  
 Cardelli, J.A., Clayton, G.C., Mathis, J.S., 1989, ApJ, 345, 245  
 Cash, W., 1979, ApJ, 228, 939  
 Collin-Souffrin, S., Alloin, D., & Andritat, Y. 1973, A&A, 22, 343  
 Condon, J. J., Cotton, W. D., Greisen, E. W., et al. 1998, AJ, 115, 1693  
 Dong, X., Wang, T., Wang, J., et al. 2008, MNRAS, 383, 581  
 Graham, M. J., Ross, N.P., Stern, D., et al. 2020, MNRAS, 491, 4925  
 Denney, K. D., De Rosa, G., Croxall, K., et al. 2014, ApJ, 796, 134  
 Edelson, R., et al. 2002, ApJ, 568, 610  
 Edelson, R., et al. 2015, ApJ, 806, 129  
 Eracleous, M., & Halpern, J.P. 1994, ApJS, 90, 1  
 Fausnaugh, M.M. et al. 2016, ApJ, 821, 56  
 Gaskell, C. M. 2017, MNRAS, 467, 226  
 Gaskell, C. M., & Harrington P.Z. 2018, MNRAS, 478, 1660  
 Gehrels, N., et al. 2004, ApJ, 611, 1005  
 Graham, M. J., Ross, N.P., Stern, D., et al. 2020, MNRAS, 491, 4925  
 Grupe, D., Komossa, S., Leighly, K. M., & Page, K.L., 2010, ApJS, 187, 64  
 Grupe, D., Thomas, H.-C., & Beuermann, K., 2001, A&A, 367, 470  
 Grupe, D., Wills, B.W., Leighly, K. M., et al. 2004, AJ, 127, 156  
 Guainazzi, M. 2002, MNRAS, 329, L13  
 Hill, J.E., et al., 2004, SPIE, 5165, 217  
 Jones, D.H., Saunders, W., Colless, M., et al. 2004, MNRAS, 355, 747  
 Kalberla, P.M.W., Burton, W.B., Hartmann, D., et al. 2005, A&A, 440, 775  
 Kollatschny, W. 2003, A&A, 407, 461  
 Kollatschny, W., Bischoff, K., Dietrich, M. 2000, A&A, 361, 901  
 Kollatschny, W., Bischoff, K., Robinson, E. L., Welsh, W. F., Hill, G. J. 2001, A&A, 379, 125  
 Kollatschny, W., & Fricke, K. J., 1985, A&A, 146, L11  
 Kollatschny, W., Ochmann, M. W., Zetzl, M. et al. 2018, A&A, 619, 168  
 Kollatschny, W., & Zetzl, M. 2010, A&A, 522, 36  
 Kollatschny, W., Zetzl, M., & Dietrich, M. 2006, A&A, 454, 459  
 Komossa, S., Zhou, H., Wang, T., et al. 2008, ApJ, 678, L13  
 LaMassa, S.M., Cales, S., Moran, E. C., et al. 2015, ApJ, 800, 144  
 Lawrence, A. 2018, NatAs, 2, 102  
 Loveday, J. 1996, MNRAS, 278, 1025  
 MacLeod, C. L., Green, P. J., Anderson, S.F., et al. 2019, ApJ, 874, 8  
 Mahony, E.K., Croom, S.M., Boyle, B. J. et al. 2010, MNRAS, 401, 1151  
 Noda, H., & Done, C. 2018, MNRAS, 480, 3898  
 Nicastro, F., Martocchia, A., & Matt, G. 2003, ApJL, 589, L13  
 Oknyansky, V. L., Winkler, H., Tsygankov, S.S., et al. 2019, MNRAS, 483, 558  
 Osterbrock, D.E., & Ferland, G.J. 2006, 'Astrophysics of Gaseous Nebulae and Active Galactic Nuclei', University Science Books  
 Park, T., Kashyap, V.L., Siemiginowska, A., van Dyk, D.A., Zezas, A., Heinke, C., & Wargelin, B.J., 2006, ApJ, 652, 610  
 Parker, M. L., Komossa, S., Kollatschny, W., et al. 2016, MNRAS, 461, 1927  
 Parker, M. L., Schartel, N., Grupe, D., et al. 2019, MNRAS, 483, L88  
 Penston, M. V., & Perez, E. 1984, MNRAS, 211, 33

- Poole, T.S. et al. 2008, MNRAS, 383, 627
- Rodríguez-Pascual P.M., Alloin D., Clavel J., et al., 1997, ApJS 110, 9
- Roming, P.W.A., et al. 2005, Space Science Reviews, 120, 95
- Ross, N. P., Ford, K.E.S., Graham, M., et al. 2018, MNRAS, 480, 4468
- Rumbaugh, N., Shen, Y. Morganson, E., et al. 2018, ApJ 854, 160
- Schlaflly E.F., & Finkbeiner, 2011, ApJ 737, 103
- Schlegel, D.J., et al. 1998, ApJ 500, 525
- Shapovalova, A. I., Popovic, L. C., Burenkov, A.N., et al. 2010, A&A, 517, A42
- Shapovalova, A. I., Popovic, L. C., Burenkov, A.N., et al. 2013, A&A, 559, 10
- Shappee, B. J., Prieto, J. L., Grupe, D., et al. 2014, ApJ, 788, 48
- Shen, Y., Ho, L. 2014, Nature, 513, 210
- Shectman, S. A., Landy, S. D., Oemler, A., et al. 1996, ApJ, 470, 172
- Shuder, J. M. 1982, ApJ, 259, 48
- Stern, D., McKernan, B., Graham, M.J., et al. 2018, ApJ, 864, 27
- Storchi-Bergmann, T., Eracleous, M., Ruiz, M.T., et al. 1997, ApJ, 489, 87
- Strateva, I., Strauss, M.A., Hao, L., et al. 2003, AJ, 126, 1720
- Sulentic, J.W., Zwitter, T., Marziani, P., et al. 2000, ApJL, 536, L5
- Tohline, J.E., Osterbrock, D. 1976, ApJ, 210, L120
- Trakhtenbrot, B., Arcavi, I., MacLeod, C.L., et al. 2019, ApJ, 883, 94
- Wang, J., Xu, D.W., Wang, Y., et al. 2019, ApJ, 887, 15
- Zetzl, M., Kollatschny, W., Ochmann, M. W., et al. 2018, A&A, 618, 83

## **Appendix A: Additional tables**

**Table A.1.** XRT and UVOT monitoring observation log: Julian date, UT date, and XRT and UVOT exposure times in seconds.

Julian date 2 400 000+	UT date (middle of the exposure)	XRT	V	B	U	UV W1	UV M2	UVW2
54266.6750	2007-06-15 04:12	5037	—	—	—	—	—	4970
54312.9792	2007-07-31 11:30	6213	—	—	6127	—	—	—
54361.9743	2007-09-18 11:23	15767	—	—	—	—	—	—
54363.0389	2007-09-19 12:56	6645	—	—	—	—	—	—
54364.1139	2007-09-20 14:44	8616	—	—	—	—	—	—
54676.7875	2008-07-29 06:54	1095	104	104	104	208	114	417
55092.9722	2009-09-18 11:20	17422	—	—	—	—	—	—
56493.4166	2013-07-20 10:13	1461	119	119	119	237	340	475
56556.3861	2013-09-20 21:16	522	44	44	44	87	114	176
57578.0396	2016-07-08 12:57	6263	84	85	84	168	260	5509
57856.3778	2017-04-12 21:04	1141	47	47	47	94	134	188
57865.0097	2017-04-21 12:14	1111	84	84	84	169	295	337
57880.7952	2017-05-07 07:05	936	78	78	78	154	222	309
57891.6903	2017-05-18 04:34	629	48	48	48	97	180	195
57895.1028	2017-05-21 14:28	946	74	74	74	150	222	301
57896.0243	2017-05-23 00:35	962	80	80	80	158	234	317
57902.8451	2017-05-29 08:17	979	80	80	80	160	245	321
57909.5556	2017-06-05 01:20	202	—	31	31	64	—	58
57913.2708	2017-06-08 18:30	924	74	74	74	148	223	297
57916.4201	2017-06-11 22:06	1898	136	136	136	510	401	544
57923.4986	2017-06-18 23:59	941	26	79	79	158	210	317
57931.2806	2017-06-26 18:44	445	37	37	37	76	90	151
57938.1931	2017-07-03 16:37	799	64	64	64	127	192	257
57944.5639	2017-07-10 01:32	832	82	82	82	163	63	326

**Table A.2.** *Swift* monitoring: V, B, U, UVOT W1, M2, and W2 reddening-corrected flux in units of  $10^{-15} \text{W m}^{-2} (10^{-12} \text{ ergs s}^{-1} \text{ cm}^{-2})$ ; columns 2 to 7) and magnitudes in the Vega system (columns 8 to 13).

JD-2400000	V	B	U	UVW1	UVM2	UVW2	V	B	U	UVW1	UV M2	UVW2
(1)	(2)	(3)	(4)	(5)	(6)	(7)	(8)	(9)	(10)	(11)	(12)	(13)
54266.6750	—	—	—	—	—	7.34±0.33	—	—	—	—	—	15.09±0.05
54312.9792	—	—	10.99±0.47	—	—	—	—	—	15.11±0.05	—	—	—
54361.9743	—	—	—	—	—	—	—	—	—	—	—	—
54363.0389	—	—	—	—	—	—	—	—	—	—	—	—
54364.1139	—	—	—	—	—	—	—	—	—	—	—	—
54676.7875	21.59±1.00	17.18±0.73	11.74±0.63	9.79±0.61	10.14±0.67	8.45±0.56	14.94±0.05	15.55±0.05	15.04±0.05	15.06±0.06	15.03±0.07	15.21±0.07
55092.9722	—	—	—	—	—	—	—	—	—	—	—	—
56493.4166	16.64±0.77	12.62±0.58	6.71±0.39	4.53±0.30	3.40±0.23	3.23±0.23	15.23±0.05	15.88±0.05	15.65±0.06	15.90±0.06	16.22±0.07	16.25±0.07
56556.3861	18.82±1.15	14.27±0.78	7.54±0.51	5.44±0.27	5.33±0.49	4.23±0.33	15.09±0.07	15.75±0.06	15.52±0.07	15.70±0.08	15.89±0.10	15.97±0.09
57578.0396	16.05±0.83	11.65±0.58	5.61±0.35	3.31±0.27	2.69±0.22	2.25±0.16	15.27±0.06	16.00±0.05	15.84±0.07	16.23±0.08	16.47±0.09	16.64±0.06
57856.3778	16.85±0.84	11.21±0.68	5.14±0.40	2.51±0.25	2.53±0.27	2.10±0.21	15.22±0.07	16.01±0.07	15.94±0.08	16.54±0.11	16.54±0.12	16.72±0.10
57865.0097	15.40±0.83	11.75±0.58	5.02±0.31	2.96±0.26	2.36±0.19	2.31±0.19	15.31±0.06	15.96±0.05	15.96±0.07	16.37±0.08	16.60±0.09	16.62±0.08
57880.7952	16.17±0.88	11.94±0.58	5.77±0.35	2.78±0.24	2.30±0.21	2.16±0.19	15.26±0.06	15.94±0.05	15.81±0.07	16.43±0.08	16.64±0.10	16.69±0.09
57891.6903	16.58±1.07	12.76±0.73	5.02±0.39	2.88±0.31	2.34±0.23	2.17±0.19	15.23±0.07	15.88±0.06	15.96±0.08	16.40±0.10	16.63±0.11	16.68±0.10
57895.1028	16.93±0.94	10.87±0.60	5.06±0.31	2.34±0.28	2.38±0.22	1.98±0.17	15.21±0.06	16.04±0.06	15.95±0.07	16.62±0.10	16.61±0.10	16.79±0.09
57896.0243	15.87±0.88	11.79±0.24	5.57±0.35	2.76±0.23	2.17±0.20	2.02±0.16	15.28±0.06	15.95±0.05	15.85±0.07	16.44±0.08	16.71±0.10	16.76±0.09
57902.8451	16.93±0.88	11.70±0.58	5.06±0.31	2.63±0.23	2.66±0.22	1.94±0.16	15.21±0.06	15.96±0.05	15.95±0.07	16.50±0.09	16.49±0.09	16.81±0.09
57909.5556	—	12.47±0.83	4.91±0.43	2.54±0.29	—	1.72±0.26	—	15.89±0.07	15.98±0.10	16.53±0.12	—	16.94±0.17
57913.2708	17.29±0.94	11.79±0.58	4.67±0.31	2.36±0.22	2.38±0.21	2.05±0.17	15.19±0.06	15.95±0.05	16.04±0.07	16.61±0.09	16.61±0.10	16.75±0.09
57916.4201	16.05±0.76	11.21±0.48	5.14±0.27	2.67±0.17	2.29±0.16	1.97±0.15	15.27±0.05	16.01±0.05	15.93±0.06	16.48±0.07	16.65±0.08	16.79±0.08
57923.4986	16.46±0.88	11.65±0.58	5.14±0.31	2.69±0.21	2.34±2.19	2.11±0.17	15.24±0.06	15.97±0.05	15.94±0.07	16.47±0.08	16.62±0.10	16.72±0.09
57931.2806	16.05±0.48	11.99±0.73	5.38±0.43	2.66±0.30	2.23±0.30	2.10±0.22	15.26±0.08	15.94±0.07	15.89±0.09	16.48±0.11	16.68±0.15	16.72±0.11
57938.1931	17.17±1.00	12.67±0.68	4.59±0.31	2.73±0.26	2.02±0.20	1.97±0.17	15.19±0.06	15.88±0.06	16.06±0.08	16.45±0.09	16.78±0.11	16.79±0.09
57944.5639	15.64±0.83	12.09±0.58	4.67±0.33	2.66±0.25	1.84±0.22	2.02±0.16	15.29±0.06	15.93±0.05	16.04±0.07	16.48±0.08	16.89±0.19	16.66±0.08



**Table A.3.** *Swift* monitoring: Julian date, UT date, XRT 0.3–10 keV count rates (CR), and hardness ratios (HR<sup>1</sup>), X-ray photon index  $\Gamma$ , the observed 0.3–10 keV X-ray flux in units of  $10^{-12}$  erg s<sup>-1</sup> cm<sup>-2</sup>, and reduced  $\chi^2$  of the simple power-law model fit (pl).

Julian Date 2400 000+	CR	HR	$\Gamma_{\text{pl}}$	XRT flux	$(\chi^2/\nu)_{\text{pl}}$
54266.6750	0.288±0.008	+0.208±0.024	1.88±0.08	11.38±0.26	39.8/50
54312.9792	0.215±0.006	+0.178±0.028	1.96±0.08	8.29±0.31	47.0/49
54361.9743	0.076±0.003	+0.266±0.033	1.78±0.09	3.10±0.14	48.7/42
54363.0389	0.079±0.004	+0.386±0.051	1.67±0.14	3.51±0.25	11.4/18
54364.1139	0.072±0.003	+0.255±0.044	1.89±0.11	2.81±0.09	25.9/23
54676.7875	0.268±0.017	+0.311±0.055	1.70±0.17	11.45±0.07	121/152 <sup>5</sup>
55092.9722	0.315±0.005	+0.138±0.015	2.04±0.04	11.46±0.02	216.0/163
56493.4166	0.067±0.007	+0.305±0.096	1.82±0.29	2.91±0.35	65.1/74 <sup>5</sup>
56556.3861	0.137±0.017	+0.241±0.127	1.92±0.39	5.09±0.92	49.5/50 <sup>5</sup>
57578.0396	0.048±0.003	+0.345±0.056	1.77±0.16	2.10±0.24	149.4/172 <sup>5</sup>
57856.3778	0.041±0.009	+0.294±0.159	1.78±0.47	1.65±0.33	27.7/33 <sup>5</sup>
57865.0097	0.035±0.007	+0.057±0.177	2.04±0.62	1.35±0.40	19.0/24 <sup>5</sup>
57880.7952	0.037±0.007	+0.562±0.136	2.30±1.02	2.48±0.16	18.4/26 <sup>5</sup>
57891.6903	0.035±0.011	+0.383±0.232	—	1.43±0.42 <sup>6</sup>	—
57895.1028	0.033±0.006	+0.554±0.153	1.77±0.58	1.41±0.45	12.2/22 <sup>5</sup>
57896.0243	0.024±0.006	-0.224±0.241	2.25±0.67	1.96±0.34	16.8/16 <sup>5</sup>
57902.8451	0.018±0.007	+0.348±0.310	—	0.67±0.27 <sup>6</sup>	—
57909.5556	0.017±0.013	—	—	0.65±0.50 <sup>6</sup>	—
57913.2708	0.026±0.006	-0.002±0.220	2.52±0.66	1.30±0.32	14.0/16 <sup>5</sup>
57916.4201	0.019±0.004	+0.028±0.200	2.01±0.89	0.33±0.12	15.2/28 <sup>5</sup>
57923.4986	0.016±0.005	-0.211±0.310	—	0.62±0.29 <sup>6</sup>	—
57931.2806	0.014±0.007	—	—	0.54±0.27 <sup>6</sup>	—
57938.1931	0.017±0.006	+0.056±0.190	—	0.65±0.23 <sup>6</sup>	—
57944.5639	0.020±0.006	+0.435±0.221	—	0.77±0.23 <sup>6</sup>	—

<sup>1</sup> The hardness ratio is defined as  $\text{HR} = \frac{\text{hard}-\text{soft}}{\text{hard}+\text{soft}}$ , where soft and hard are the background-corrected counts in the 0.3–1.0 keV and 1.0–10.0 keV bands, respectively

<sup>2</sup> The intrinsic  $N_{\text{H, intr}}$  is given in units of  $10^{21}$  cm<sup>-2</sup>

<sup>3</sup> No additional absorber required. The fit is consistent with Galactic absorption alone.

<sup>4</sup> These observations were performed in windowed timing mode.

<sup>5</sup> Fit using Cash statistics (Cash 1979)

<sup>6</sup> Extrapolated from the XRT count rates using the flux and count rate of the MJD 57865 observation